APPLIED PHYSICS

Steering valley-polarized emission of monolayer MoS_2 sandwiched in plasmonic antennas

Te Wen[1,2], Weidong Zhang[1,2], Shuai Liu[1], Aiqin Hu[1], Jingyi Zhao[1], Yu Ye[1], Yang Chen[3], Cheng-Wei Qiu[3]*, Qihuang Gong[1,2], Guowei Lu[1,2]*

Monolayer transition metal dichalcogenides have intrinsic spin-valley degrees of freedom, making it appealing to exploit valleytronic and optoelectronic applications at the nanoscale. Here, we demonstrate that a chiral plasmonic antenna consisting of two stacked gold nanorods can modulate strongly valley-polarized photoluminescence (PL) of monolayer MoS_2 in a broad spectral range at room temperature. The valley-polarized PL of the MoS_2 using the antenna can reach up to ~47%, with approximately three orders of PL magnitude enhancement within the plasmonic nanogap. Besides, the K and K′ valleys under opposite circularly polarized light excitation exhibit different emission intensities and directivities in the far field, which can be attributed to the modulation of the valley-dependent excitons by the chiral antenna in both the excitation and emission processes. The distinct features of the ultracompact hybrid suggest potential applications for valleytronic and photonic devices, chiral quantum optics, and high-sensitivity detection.

INTRODUCTION

Broken inversion symmetry and strong spin-orbit interaction in monolayer transition metal dichalcogenides (TMDCs) lead to spin-valley locking at K and K′ valleys (*1*–*3*). Energetically degenerate excitons in different valleys can be optically addressed and detected using different circularly polarized light because of their valley-dependent optical selection rule (*4*–*6*). As a result, the spin-valley effect lays the foundation for the exploration of valleytronics (*7*–*9*). Metallic nanostructures [e.g., nanowires (*10*), gratings (*11*), and metasurfaces (*12*–*16*), etc.] have been used to improve the light-matter interaction and steer valley-polarized emission of TMDCs. These nanostructures can spatially separate the emission of valley excitons through the near-field interference of circularly polarized dipoles, resulting in asymmetric emission. These waveguide structures provide a feasible way to design valleytronic devices by combining TMDCs with nanophotonic structure.

Nevertheless, previous metallic nanostructure–based surface plasmon polaritons used to control valley emission have had large footprints on the microscale. It is well known that localized surface plasmon resonance (LSPR) can concentrate the electromagnetic field considerably in a tiny volume to improve the light-matter interaction on the nanoscale. Nano-objects such as metallic core-shell, V-shaped, and Yagi-Uda antennas have been shown to control the emission directivity of nanoemitters (*17*–*20*); however, these antennas have seldom been applied to valleytronic devices. Chiral light-matter interactions in valleytronic applications need a chiral structure to generate chiral electromagnetic near fields (*21*, *22*). Chiral nanostructures have been widely applied in the study of biomolecules through the analysis of circular dichroism spectra, providing valuable information with high sensitivity (*23*–*25*). Recently, chiral MoS_2-metasurface heterostructures have been used to tailor the valley-polarized photoluminescence (PL) of monolayer MoS_2 (*12*). However, the chiral performance was only successfully achieved at low temperatures down to 87 K because of the low coupling efficiency between the metasurfaces and valley excitons in MoS_2, limiting its application at room temperature.

In this study, we constructed a stereoscopic antenna consisting of two gold nanorods (GNRs) with a small footprint (~0.02 μm^2) and an ultrasmall "hot-spot" volume. We experimentally assembled two GNRs in a corner-stacked configuration to form the stereoscopic antenna via atomic force microscopy (AFM) manipulation. The monolayer MoS_2 was sandwiched inside the nanogap to greatly enhance the interaction between the LSPRs and excitons. Compared with previous works, this stereoscopic antenna having chiral properties can more efficiently tailor valley-polarized emission of monolayer MoS_2, reaching up to a degree of valley polarization (DVP) of ~47% at room temperature (Fig. 1A). We observed that the PL valley polarization of the MoS_2 was dependent on the configurations of the antennas. In addition, the chiral antenna can modulate the emission directions of the MoS_2 over a broad spectral range, and even unidirectional emission could occur. The PL emission of valley excitons under different polarized excitations can be separated spatially. Combining the finite-difference time-domain (FDTD) method and the dipole-dipole model, we revealed that the far-field interference between the radiation fields from the MoS_2 and the out-of-phase dipoles induced in the GNRs gave rise to this unidirectional emission effect. The valley-polarized modulation originates from the near-field interaction between excitons of the monolayer MoS_2 and the chiral field of the antenna. The calculated results, such as the electromagnetic distribution field, antenna quantum efficiency, and optical chirality, supported the experimental observations.

RESULTS

The valley-dependent selection rule can explain the chiral optical valley selectivity of the PL of MoS_2. In a MoS_2 monolayer, the coupling of right-/left-handed circularly polarized (RCP/LCP) light with the K/K′ valley to generate valley excitons leads to opposite-handed

[1]State Key Laboratory for Mesoscopic Physics, Frontiers Science Center for Nano-optoelectronics, and Collaborative Innovation Center of Quantum Matter, School of Physics, Peking University, Beijing 100871, China. [2]Collaborative Innovation Center of Extreme Optics, Shanxi University, Taiyuan, Shanxi 030006, China. [3]Department of Electrical and Computer Engineering, National University of Singapore, Singapore 117583, Singapore.
*Corresponding author. Email: chengwei.qiu@nus.edu.sg (C.-W.Q.); guowei.lu@pku.edu.cn (G.L.)

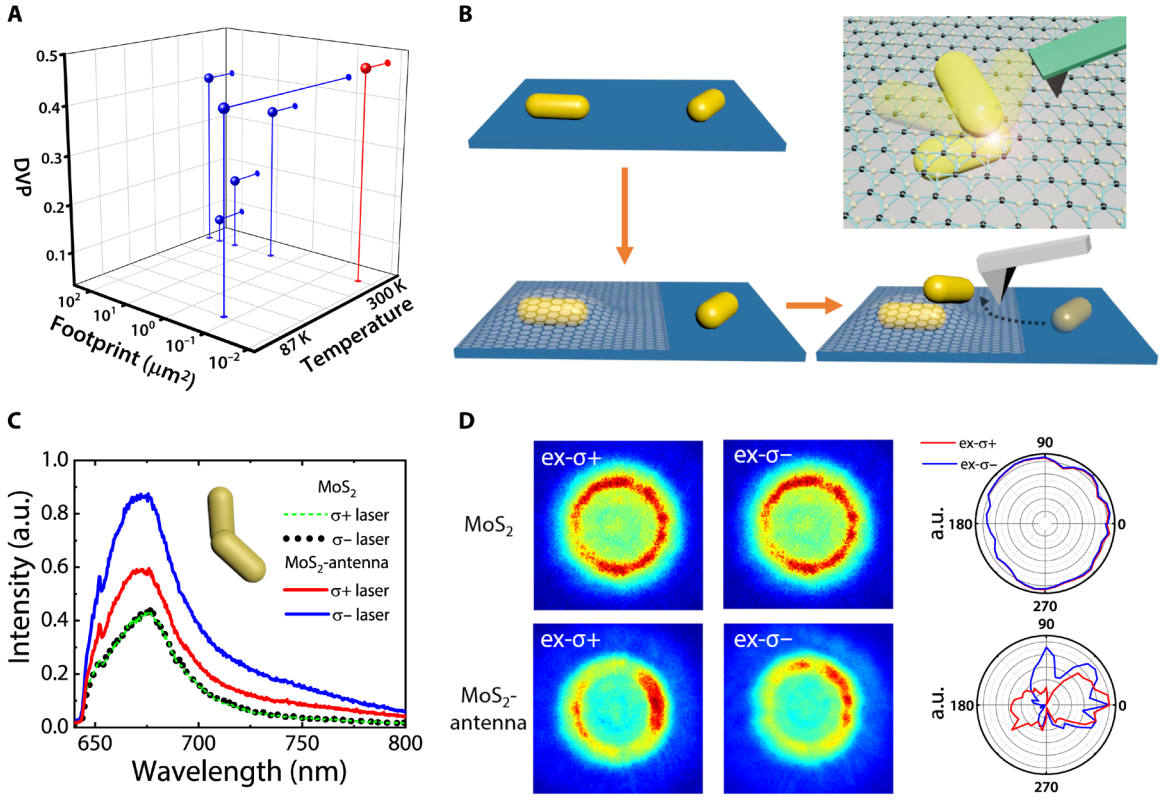

Fig. 1. Valley-controlled PL results of MoS_2-antenna hybrid. (**A**) Representative examples (*10*–*12*, *15*, *16*) of chiral metallic nanostructures to improve the light-matter interaction and steer the valley-polarized emission of TMDCs (blue balls). The performances were characterized by the DVP, footprint, and experimental temperature. The present stereoscopic antennas exhibited excellent chirality to form a valleytronics device with a small footprint and high DVP working at room temperature, as indicated by the red ball. (**B**) Schematic illustrations of a representative stereoscopic antenna with monolayer MoS_2 sandwiched in the nanogap between two GNRs. (**C**) PL spectra for typical MoS_2 monolayer (dots) and an LH antenna–MoS_2 hybrid (lines) under circularly polarized excitation. a.u., arbitrary units. (**D**) Measured far-field PL patterns and corresponding normalized angular radiation distributions in polar coordinates for the bare MoS_2 monolayer and the LH antenna–MoS_2 hybrid.

circularly polarized emission. Because of phonon-assisted intervalley scattering, excitons can partly scatter into the opposite valley. In the present experiment, the pristine monolayer MoS_2 without antenna exhibited 18% DVP at room temperature. For symmetric metal structures such as a single GNR, the near-field enhancement is chirality independent. The excitons of opposite valleys couple equally to the local field of such achiral plasmonic structures that cannot modify the DVP. To obtain a chiral antenna, we had to break the symmetry of the nanostructures. The MoS_2-antenna hybrid was assembled using the AFM manipulation method. The top-right illustration in Fig. 1B presents a schematic of the chiral stereoscopic plasmonic antenna in the present experiment, which consists of two GNRs with corner-stacked configuration and a MoS_2 monolayer sandwiched in the nanogap. First, the GNRs were sparsely deposited on a glass coverslip with separations of several micrometers, as confirmed by AFM and optical images. Then, the chemical vapor deposition (CVD)–grown MoS_2 monolayer was transferred onto the coverslip. Last, with the aid of AFM manipulations, we assembled the chiral antenna by moving a GNR from the bare glass onto a GNR covered by monolayer MoS_2. We then adjusted the relative position and intersection angle between the two stacked GNRs, which determined the chirality and optical response of the antenna (*26*–*28*). During the manipulation, we measured their optical properties in situ, which was convenient for studying the optical response of the hybrids with different configurations. Representative images of the AFM manipulation during the assembly process are presented in fig. S1A. We defined this structure as a left-handed (LH) antenna. Figure 1C presents the PL spectra of monolayer MoS_2 with and without the antenna at room temperature. The emission intensity of valley excitons was enhanced markedly and had a higher enhancement factor under σ− polarized excitation than under σ+ polarized excitation for the LH antenna. In addition, we observed different directivities under oppositely polarized excitation for the MoS_2 with the antenna, as shown in the far-field angular patterns (Fig. 1D), with unidirectional emission even exhibited to some extent. For comparison, the far-field emission patterns of the bare MoS_2 monolayer are shown in Fig. 1D, with a uniform angular distribution observed because of the isotropic response of the excitons.

We measured the PL emission patterns using the back focal plane (BFP) imaging method, as shown in the schematic in Fig. 2A. For comparison, the PL emission patterns of a hybrid consisting of the MoS_2 and a single GNR were also measured (as shown in fig. S2). Because of the symmetrical shape of the individual GNR, there was no chiral characteristic according to the emission patterns, and the directivity was dominated by the dipolar-like mode of the GNR. When two GNRs were assembled to form a stereoscopic V-shaped antenna, the unidirectional emission patterns appeared

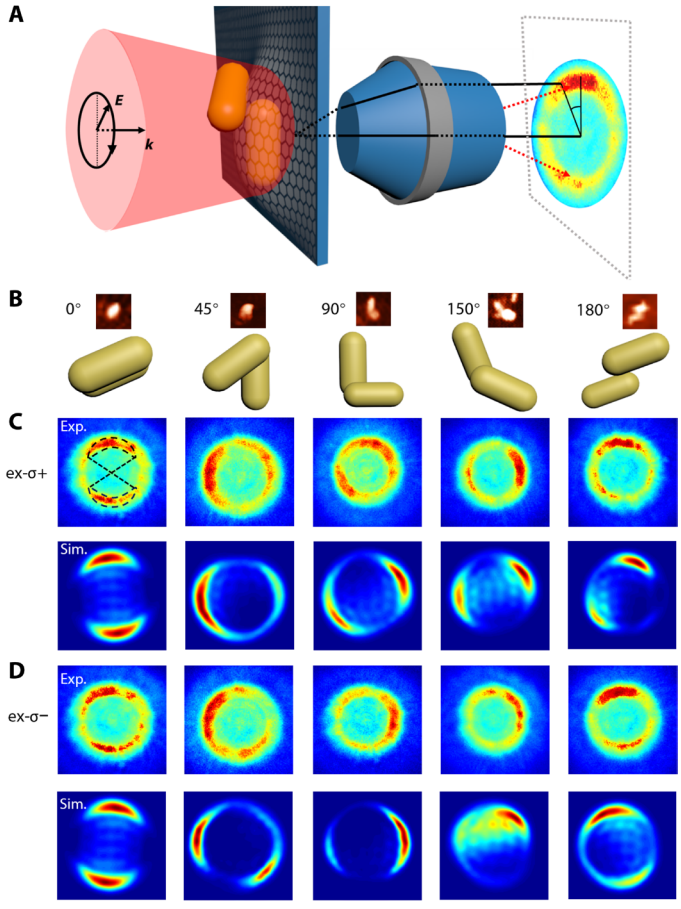

Fig. 2. Directional emission measurements of monolayer MoS_2 modified using the LH antenna with different intersection angles under σ+/σ− polarized excitation. (**A**) Schematic design of experimental setup using BFP imaging. (**B**) AFM scanning images and corresponding schematic diagrams for antennas with different configurations. (**C** and **D**) Experimental far-field PL patterns under σ+ (C)/σ− (D) polarized excitation and corresponding simulated far-field emission patterns obtained using the FDTD method.

for a series of LH antennas, as observed in Fig. 2 (C and D). Regarding the LH antenna with an intersection angle ~0°, 45°, 90°, 150°, or 180°, the PL patterns under σ+/σ− polarized excitation differed from each other. Because the area of the laser focus spot was much larger than the area affected by the antenna, most of the MoS_2 was excited directly by the light without any effect of the antenna, resulting in a background in the experiment. For estimation of the background signal, the section area of the antenna, and the laser spot size, see section S1. The modulation of chiral emission occurred mainly within the near field around the antenna, where excitons interacted strongly with plasmon modes. To quantify the unidirectional emission induced by the hybrid, we accounted for the background emission and subtracted the raw data with the background signal using a ratio of $1 - \frac{S_c}{S_0}$, where S_c and S_0 are the extinction cross-sectional area of the antenna and the area of the laser spot, respectively. $\frac{S_c}{S_0}$ was estimated to be 11.4% in the present experiment (details in section S1 and fig. S3). We introduce the directivity, D, as the ratio between the maximum emitted power on a side and its opposite side in the BFP patterns: $D = 10 \times \log_{10}\frac{\sum S_1}{\sum S_2}$. The directivity values S_1 and S_2 were obtained by integrating the PL intensities over two different areas shown in the first image of Fig. 2C (dashed lines) after background correction. From the quantitative values in fig. S4, we observed that the directional emission performance changed with opposite circular polarization excitation and the intersection angle. Moreover, the PL patterns of the hybrid structure under different linear polarized excitation (fig. S5) also changed because of the structural chirality of the antenna.

In addition to the experiments, we calculated the far-field emission patterns by using the FDTD method (*29*) and the near-field–to–far-field (NFTFF) transformation method. The emission from the MoS_2 monolayer originates solely from the in-plane excitons at K and K′ valleys (*30*). Thus, the valley exciton emission can be treated as dipole pairs at a wavelength of 675 nm (A exciton of MoS_2) polarized perpendicular to each other in the X-Y plane with a phase difference of ±90° for σ+/− polarized emission. As shown in Fig. 3A, we placed a dipole pair in the hot spot for simplicity. We determined the physical size of the antenna shown in Fig. 3A from AFM measurements and FDTD simulations (as discussed in section S1). The calculated angular emission patterns for different configurations are presented in Fig. 2 (C and D). The difference in the far-field angular distribution under oppositely circular-polarized excitation results from the different chiral near-field response in the nanogap. We note that there are some deviations between the experimental and simulated results, which can be attributed to the deviations between the simulation and experiment, such as the exciton distribution and quantity and the antenna configuration resulting from different separation and orientation of the GNRs. For example, the top GNR was oblique in the experiment (as discussed in fig. S1), whereas the GNR was set as horizontal in the simulations.

To understand the unidirectional emission, we used the FDTD method and the dipole-dipole model (*31*) to simulate the processes. Such unidirectional emission can be explained as the interference of the direct radiation from the monolayer MoS_2 with the radiation from the induced dipolar mode of the antenna. The dipole moment can be written as $P_j = P_{xj}e^{i\varphi_x} + P_{yj}e^{i\varphi_y}$, where j = 1 and 2 refer to the two dipoles, and x and y refer to the component in the X and Y directions. Thus, the constructive or destructive interference depends on the relative amplitude (P_1/P_2) and phase difference ($\Delta\varphi \pm kl$) of the two dipole moments, where k is the wavelength vector and l is the dipole-dipole separation distance. Figure 3B presents a schematic illustration of the model for the analysis of directional emission. In this case, the constructive or destructive interference in the x/y component is the bright or dark region, respectively, in the angular distribution in the X or Y direction. For destructive interference, the two conditions, i.e., $P_1/P_2 = 1$ and $|\Delta\varphi \pm kl| = \pi$, should be satisfied in the same direction, resulting in unidirectional emission (the calculations are described in detail in section S2). For the antenna in Fig. 3A, the surface charge-density distributions around two GNRs were transferred to the plane of the dipole pair by adding a phase of kd_1 and kd_2, where d_1 = 45 nm and d_2 = −32.5 nm. The surface charge-density distribution of the σ− dipole pair is shown in Fig. 3C. The calculated results indicate that the total phase difference in the Y direction is $\Delta\varphi_x + kl_x = 1.026\pi$ and $P_{1x}/P_{2x} = 1.27$, which suppresses the radiation in the $-Y$ direction (resulting in unidirectional emission D of ~8.4 dB). In the X direction, the parameters were far from the destructive interference conditions, with equal radiation in both the ±X directions (~1.6 dB). For comparison, the surface charge-density distribution and calculated results with a σ+ dipole pair in the same plane in Fig. 3 (E and F) explain

the directional emission pattern. These results illustrate the origin of the directional emission under opposite polarization excitation.

Furthermore, we compared the valley-polarized PL spectra of the pristine MoS_2 and MoS_2-antenna hybrid. The representative polarized PL spectra of the pristine MoS_2 show similar behaviors for the LCP and RCP excitations in fig. S6. The obtained DVP (~18%) is consistent with that in previous works, with typical values of DVP of 15 to 25% at room temperature (*32*). This result was expected under the valley-dependent optical selection rule. As discussed above, the excitons directly excited by the laser contribute to the background signal. We accounted for the background to obtain an accurate result of the chiral emission by subtracting the background [approximately 88.6% of the intensity of the pristine MoS_2 shown in fig. S6 (A and B)]. The corresponding PL spectra after background corrections are presented in Fig. 4 (A and B) for opposite chiral polarized excitations. We calculated DVP = $\frac{I(\sigma-)-I(\sigma+)}{I(\sigma-)+I(\sigma+)}$ in the valley-polarized PL to evaluate the performance. The absolute value of DVP of the hybrid reached up to ~47% under σ− excitation but decreased to 11% under σ+ excitation near the A exciton of MoS_2 (675 nm). Compared with the pristine MoS_2, that with the antenna resulted in brighter emission with σ− polarization excitation and a higher proportion of σ− PL emission. For comparison, the valley-polarized PL spectra of the MoS_2 coupled with a single GNR are presented in fig. S2. The absolute values of DVP with σ+/σ− polarized excitation are similar (DVP, ~21%) because of the chirality-independent localized field of a single GNR. As mentioned above, the relative position of the intersection between the stacked GNRs determines the chirality and optical response of the antenna. We constructed another representative antenna with opposite chirality [right-handed (RH)] as that of the LH antenna discussed above, as shown in fig. S7. The conclusions drawn from the LH antenna and associated mechanisms were equivalent to those for the RH antenna. This result indicates that we can obtain valleytronic devices with a certain helicity by controlling the configuration using the AFM manipulation method.

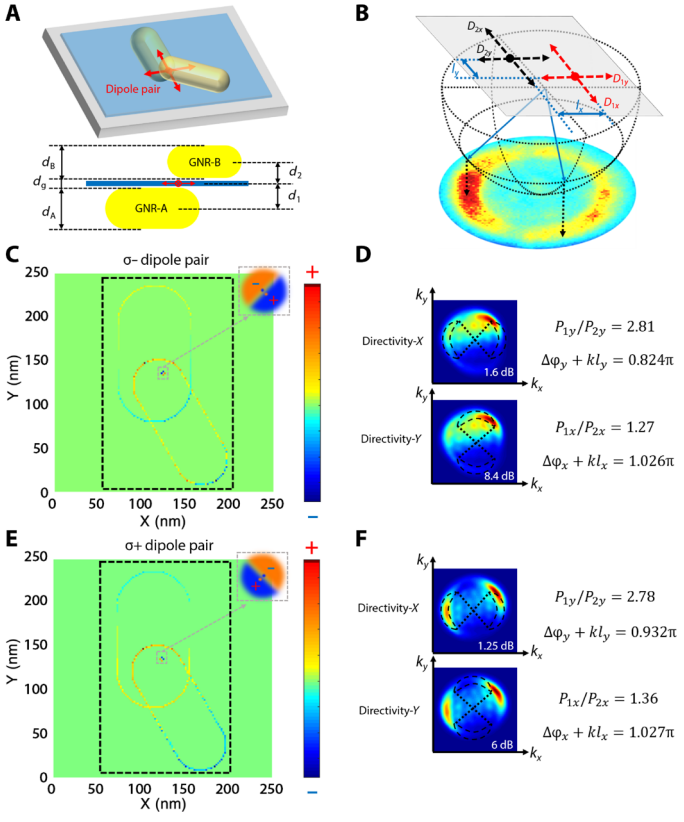

Fig. 3. Simulations of the physical origin of far-field directional emission. (**A**) Scheme of calculation of far-field directional emission modified using the LH antenna. Top and bottom: top and side views of the structure, respectively. Yellow, GNRs. Blue, MoS_2 monolayer. d_A, diameter of GNR-A (85 nm); d_B, diameter of GNR-B (60 nm); d_g, the nanogap distance between GNRs (5 nm); d_1 and d_2, distances between the centerline of the GNRs and MoS_2 (45 and 32.5 nm, respectively). (**B**) Schematic illustration of the dipole-dipole model. D_{1x} and D_{1y} represent the *x*/*y* components of the dipole pair's moment, and D_2 represents the induced dipole of the antenna. l_x and l_y represent the dipole-dipole separations between D_1 and D_2. (**C** and **E**) Simulated charge-density distributions in the *X*-*Y* plane. The dashed lines indicate the integrating regions for dipole moments D_1 (gray) and D_2 (black). (**D** and **F**) Analysis of the directivities of simulated far-field emission patterns with a σ− (D)/σ+ (F) dipole pair. Left: The far-field emissions calculated using the FDTD method. The simulated emission directivities were obtained by integrating the emission intensities over the two opposite intervals shown in the picture (black dotted lines). Right: Corresponding calculated results obtained using the dipole-dipole model.

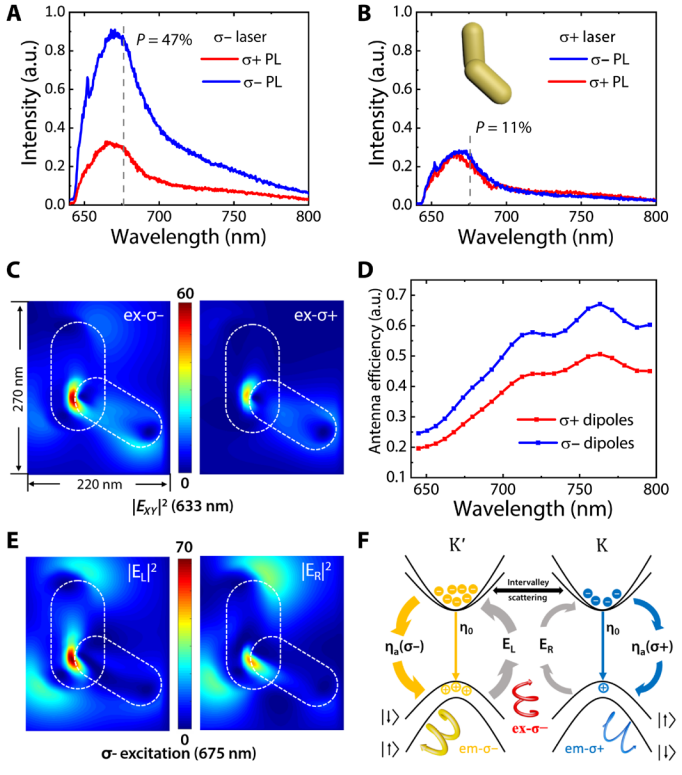

Fig. 4. Valley-polarized PL measurements and FDTD simulations of LH antenna–MoS_2 hybrid. (**A** and **B**) σ+ (red) and σ− (blue) polarized PL spectra of LH antenna–MoS_2 hybrid under σ− (A) and σ+ (B) polarization excitation. (**C**) Electromagnetic field distribution under σ− and σ+ excitation at 633 nm at $Z = 45$ nm. (**D**) The antenna efficiency for the σ+ (red) and σ− (blue) dipole pairs as a function of wavelength. (**E**) Simulated E_L and E_R components at a wavelength of 675 nm in the near-field distribution under σ− polarization excitation. (**F**) Schematic illustrations of the modulation of valley exciton PL process using the LH antenna under σ− polarization excitation.

DISCUSSION

It is well known that an antenna can increase the localized excitation field to enhance the PL intensity and radiative decay rate of excitons through the Purcell effect (*33*–*35*). We measured the PL intensity with the antenna (PL_{with}) and without the antenna ($PL_{w/o}$), as shown in Fig. 1C. Taking S_h as the hot-spot averaged area for effective enhancement, the PL enhancement factor f_{PEF} was calculated using $f_{PEF} \sim \frac{S_0}{S_h}\left(\frac{PL_{with}}{PL_{w/o}} - 1\right)$ (details in section S1), where S_0 is the focus area. We obtained f_{PEF} of ~300 for σ+ polarized excitation and ~950 for σ− polarized excitation at a wavelength of 675 nm. In the simulations, the relative PL enhancement factor was estimated using $g_{PL} = g_{ex} \times g_{em} = |E/E_0|^2 \times |\eta/\eta_0|$, where $g_{ex} = |E/E_0|^2$ is the in-plane excitation field enhancement at an excitation wavelength of 633 nm and $g_{em} = |\eta/\eta_0|$ is the enhancement of the quantum yield at an emission wavelength of 675 nm. Figure 4C shows the relative intensity of the in-plane electromagnetic field at the excitation wavelength with opposite polarization excitation at $Z = 45$ nm, where the equivalent MoS_2 layer was placed. E_{XY} showed higher enhancement and a broader distribution with σ− polarized excitation than with σ+ polarized excitation. Then, we placed 16 dipole pairs with a phase difference of ±90° in the nanogap with random phases and positions for chiral emission simulation. η(ω) is related to $\eta_0(\omega)$ (the original quantum efficiency of MoS_2), $\eta_a(\omega)$ (the antenna quantum efficiency), and $F(\omega)$ (the radiative decay rate enhancement, i.e., the Purcell factor) according to $\eta(\omega) = \eta_0(\omega)/\left[\frac{1-\eta_0(\omega)}{F(\omega)} + \frac{\eta_0(\omega)}{\eta_a(\omega)}\right]$. η_a is the ratio of P_{rad} (the energy that reaches the far field) to P_{tot} (the total power dissipated by the emitter), and F is the ratio of P_{rad} to P^0_{rad} (the energy that reaches the far field without the antenna). The corresponding η_a as a function of wavelength is shown in Fig. 4E, revealing a higher quantum yield efficiency with σ− dipole pairs at a wavelength of 675 nm than that with σ+ dipole pairs. The assumed quantum efficiency of monolayer MoS_2 (η_0) at λ = 675 nm was ~1% in our simulation (*36*). After calculation, the antenna has a larger enhancement factor under σ− polarized excitation (~1620) than under σ+ polarized excitation (~630), which is roughly consistent with the experimental results.

The valley helicity is strongly affected by the competition between the intervalley scattering rate (Γ_v) and the recombination rate (Γ_0) of e-h pair (*3*). The valley polarization of pure MoS_2 is depolarized mainly by intervalley scattering between K and K′ valley $\left(DVP \propto \frac{1}{1 + 2\Gamma_v/\Gamma_0}\right)$. Generally, a faster radiative decay rate will lead to a higher polarization helicity. The exciton transition from excited states to ground states can be affected strongly by the antenna through the Purcell effect (*37*), which can contribute to the increasing of valley polarization. The chiral plasmonic antenna modulates the excitons in the K or K′ valley with different decay rates and antenna efficiencies. For example, as shown in Fig. 4D, for an LH antenna, the antenna quantum efficiency for σ− dipoles ($\eta_a^- \sim 0.36$) is higher than that for σ+ dipoles ($\eta_a^+ \sim 0.27$), leading to a higher quantum yield efficiency for excitons in the K′ valley than those in the K valley. To quantify the contributions of the Purcell effect, we modeled the behaviors of valley excitons within the hot spot with steady-state rate equations (details in section S3). For the exciton transition, the modulated DVP can be written as $DVP = \frac{\eta_a^- n_- - \eta_a^+ n_+}{\eta_a^- n_- + \eta_a^+ n_+} \approx \frac{P_-\Gamma^r_{a-} - P_+\Gamma^r_{a+}}{P_-\Gamma^r_{a-} + P_+\Gamma^r_{a+}}$, where $P_\pm$ and $\Gamma^r_{a\pm}$ are the pumping rates and the radiative decay rates modulated by the antenna. Here, $\Gamma^{tot}_a \gg \Gamma_v > \Gamma_0$, and we assumed that Γ_0 and Γ_v are not influenced by the antenna since they dominantly depend on the intrinsic properties of MoS_2, ambient temperature, excitation energy, etc. We found that the antenna-assisted valley transition increases the DVP greatly (more than 90%) through the Purcell effect after calculating (details in section S3). For the LH antenna, the DVP value ($p_{\sigma-}$) by σ− excitation is higher than that ($p_{\sigma+}$) under σ+ excitation owing to the chiral efficiency effect.

However, the antenna can also strongly modify the polarization states of the light, which depolarized the DVP of the detected far-field PL signal. We can divide this depolarization effect into two processes, i.e., the excitation and emission process involving the conversions between the near field and the far field. First, the excitons generate both in the K and K′ valley even under pure circularly polarized excitation. The generation rates in the K/K′ valley are governed by the E_R and E_L components in the near field within the hot spot, which can be obtained numerically through $E_R = \frac{1}{2}(E_x + iE_y)$ and $E_L = \frac{1}{2}(E_x - iE_y)$. Under excitation using σ− polarized light, more excitons generate in the K′ valley rather than K valley because of the stronger E_L than E_R for the LH antenna (shown in Fig. 4E). For comparison, schematic illustrations of the E_L and E_R distributions and the valley-polarized modulation under σ+ excitation are shown in fig. S8. Second, after the exciton transitions, the antenna would scatter the near-field light to the far field as the detected PL signal. This scattering process also changes the DVP (discussed in section S3). Considering all these factors, we obtained the final $DVP_{\sigma-} \approx 30\%$ and $DVP_{\sigma+} \approx 10\%$ for the LH antenna under σ− or σ+ polarized light excitations, respectively. The numerical results are in reasonable agreement with the experiment result ($p_{\sigma-} = 47\%$ and $p_{\sigma+} = 11\%$). The deviations could be due to differences between the simulation and experiment such as the distribution and quantity of excitons or the antenna configuration such as different separation and orientation of the GNRs.

In addition, we calculated the optical chirality C as $C(\vec{r}) = -\frac{\varepsilon_0\omega}{2} Im[\vec{E}^*(\vec{r}) \times \vec{B}(\vec{r})]$ in the nanogap, which has been applied to describe the enhancement performance of circular dichroism signals detected from chiral chemical and biological molecules (*23*–*25*). $\vec{B}$, ε_0, and ω in this equation are the magnetic fields, the permittivity of vacuum, and angular frequency. As shown in fig. S10, C/C_0 of the chiral field is as large as 18 under σ− excitation, where C_0 is the value of optical chirality for a σ− polarized plane wave in a vacuum. C/C_0 has the opposite distribution under σ+ excitation with a maximum value of 8, indicating the intrinsic chirality for this antenna. In the experiment, the antenna can steer the valley-polarized PL of monolayer MoS_2 in a broader spectral range, with a DVP of 34 to 54% at wavelengths ranging from 640 to 800 nm. We believe that the nanogap volume would result in a strong coupling strength, which allows the chiral plasmonic effect to extend to the nonresonant range. Hence, tuning of the LSPR mode of the antenna to the exciton energy of MoS_2 was not necessary, which is beneficial for the nanofabrication of valleytronic devices based on the plasmon-TMDC hybrid system.

CONCLUSION

In summary, we demonstrated that an ultracompact chiral antenna formed by corner-stacked GNRs can efficiently tailor valley-polarized PL of monolayer MoS_2 at room temperature. With the aid of AFM, we could manipulate such plasmonic antennas with different configurations with the monolayer MoS_2 sandwiched in the nanogap. The nanogap (~5 nm) between the GNRs made it possible to steer

the valley-polarized PL of monolayer MoS_2 markedly over a broad spectral range owing to the strong interaction between the excitons and LSPRs at room temperature. Compared with that of pristine monolayer MoS_2, far-field emission of valley excitons with the stereoscopic chiral antennas exhibited unidirectional emission, accompanied by three orders of the PL magnitude enhancement within the plasmon nanogap. Our findings demonstrate the feasibility of designing an ultracompact nanoantenna to effectively modulate the valley-polarized luminescence.

MATERIALS AND METHODS

Sample preparation

In our experiments, the MoS_2 monolayer was prepared using the CVD method (*32*). The GNRs with a size of approximately 70 nm by 160 nm were synthesized using a seed-mediated wet chemical method (*38*). After the GNRs were sparsely deposited on a glass coverslip, the MoS_2 monolayer was transferred onto the glass coverslip using polydimethylsiloxane (*39*).

Experimental setup

We combined an inverted Olympus optical microscope with an atomic force microscope on the top side to scan and manipulate the GNRs. The CVD-grown MoS_2 monolayer boundary can be distinguished by the gray contrast of the AFM image in fig. S1, as indicated by the dotted line. To study the valley polarization PL of the MoS_2 monolayer, we used polarized excitation and circularly polarized PL measurements. A continuous wave laser at 633 nm was used to excite the samples passing through an oil immersion objective lens (1.4 numerical aperture, 60×; Olympus). We set a quarter-wave plate (633 nm) after the laser irradiation to obtain circularly polarized excitation. To resolve and measure the circularly polarized PL spectra, we placed a broadband quarter-wave plate (400 to 800 nm) and a Glan lens before the spectrometer. As shown in Fig. 1C, one characteristic PL peak of MoS_2 monolayer was observed in the spectrum, which was the direct bandgap transition (A exciton, 675 nm). Moreover, the far-field PL emission patterns were measured using the BFP imaging method. In addition, the scattering spectra of the same nanostructures were obtained in situ using the white-light total internal reflection dark-field method (*40*). All the measurements were performed at room temperature.

FDTD simulations

Three-dimensional (3D) FDTD methods were used to simulate the emission flux, emission patterns, and electric-field distributions of the assembled hybrid nanoantenna. The calculations of the far-field radiation pattern were based on the NFTFF transformation method. Although the NFTFF method is derived for a closed surface, here, we chose a large transformation plane (2 μm by 2 μm) placed 50 nm beneath the air/glass interface to collect most of the flux directed to the substrate to achieve a better approximation. In this 3D simulation, the mesh size is 0.5 nm to match the memory resources and computation time. The optical dielectric function of gold was modeled using the Drude-Lorentz dispersion model (*29*). The optical dielectric function of the equivalent MoS_2 layer was modeled using the experimental data in the references. In addition, the refractive indices of the media were set to 1.0 for air and 1.49 for silica (glass substrate). To form a chiral excitation, we used two plane waves polarized perpendicular to each other in the *X*-*Y* plane with a phase difference of ±90° for σ+/− polarized light. The chiral emission of monolayer MoS_2 was regarded as dipole pairs in the *X*-*Y* plane. Each dipole pair consisted of two orthogonal electrical dipoles. The phase difference of ±90° represented a σ+/− polarized exciton.

SUPPLEMENTARY MATERIALS

Supplementary material for this article is available at http://advances.sciencemag.org/cgi/content/full/6/21/eaao0019/DC1

REFERENCES AND NOTES

1. H. Zeng, J. Dai, W. Yao, D. Xiao, X. Cui, Valley polarization in MoS_2 monolayers by optical pumping. *Nat. Nanotechnol.* **7**, 490–493 (2012).
2. K. F. Mak, K. He, J. Shan, T. F. Heinz, Control of valley polarization in monolayer MoS_2 by optical helicity. *Nat. Nanotechnol.* **7**, 494–498 (2012).
3. T. Cao, G. Wang, W. Han, H. Ye, C. Zhu, J. Shi, Q. Niu, P. Tan, E. Wang, B. Liu, J. Feng, Valley-selective circular dichroism of monolayer molybdenum disulphide. *Nat. Commun.* **3**, 887 (2012).
4. D. Xiao, W. Yao, Q. Niu, Valley-contrasting physics in graphene: Magnetic moment and topological transport. *Phys. Rev. Lett.* **99**, 236809 (2007).
5. W. Yao, D. Xiao, Q. Niu, Valley-dependent optoelectronics from inversion symmetry breaking. *Phys. Rev. B* **77**, 235406 (2008).
6. J. S. Ross, S. Wu, H. Yu, N. J. Ghimire, A. M. Jones, G. Aivazian, J. Yan, D. G. Mandrus, D. Xiao, W. Yao, X. Xu, Electrical control of neutral and charged excitons in a monolayer semiconductor. *Nat. Commun.* **4**, 1474 (2013).
7. D. Xiao, G.-B. Liu, W. Feng, X. Xu, W. Yao, Coupled spin and valley physics in monolayers of MoS_2 and other group-VI dichalcogenides. *Phys. Rev. Lett.* **108**, 196802 (2012).
8. X. Xu, W. Yao, D. Xiao, T. F. Heinz, Spin and pseudospins in layered transition metal dichalcogenides. *Nat. Phys.* **10**, 343–350 (2014).
9. J. R. Schaibley, H. Yu, G. Clark, P. Rivera, J. S. Ross, K. L. Seyler, W. Yao, X. Xu, Valleytronics in 2D materials. *Nat. Rev. Mater.* **1**, 16055 (2016).
10. S.-H. Gong, F. Alpeggiani, B. Sciacca, E. C. Garnett, L. Kuipers, Nanoscale chiral valley-photon interface through optical spin-orbit coupling. *Science* **359**, 443–447 (2018).
11. L. Sun, C.-Y. Wang, A. Krasnok, J. Choi, J. Shi, J. S. Gomez-Diaz, A. Zepeda, S. Gwo, C.-K. Shih, A. Alù, X. Li, Separation of valley excitons in a MoS_2 monolayer using a subwavelength asymmetric groove array. *Nat. Photonics* **13**, 180–184 (2019).
12. Z. Li, C. Liu, X. Rong, Y. Luo, H. Cheng, L. Zheng, F. Lin, B. Shen, Y. Gong, S. Zhang, Z. Fang, Tailoring MoS_2 valley-polarized photoluminescence with super chiral near-field. *Adv. Mater.* **30**, 1801908 (2018).
13. G. Hu, X. Hong, K. Wang, J. Wu, H.-X. Xu, W. Zhao, W. Liu, S. Zhang, F. Garcia-Vidal, B. Wang, P. Lu, C.-W. Qiu, Coherent steering of nonlinear chiral valley photons with a synthetic Au–WS_2 metasurface. *Nat. Photonics* **13**, 467–472 (2019).
14. M. Thomaschewski, Y. Yang, C. Wolff, A. S. Roberts, S. I. Bozhevolnyi, On-chip detection of optical spin–orbit interactions in plasmonic nanocircuits. *Nano Lett.* **19**, 1166–1171 (2019).
15. T. Chervy, S. Azzini, E. Lorchat, S. Wang, Y. Gorodetski, J. A. Hutchison, S. Berciaud, T. W. Ebbesen, C. Genet, Room temperature chiral coupling of valley excitons with spin-momentum locked surface plasmons. *ACS Photonics* **5**, 1281–1287 (2018).
16. B. Ding, Z. Zhang, Y.-H. Chen, Y. Zhang, R. J. Blaikie, M. Qiu, Tunable valley polarized plasmon-exciton polaritons in two-dimensional semiconductors. *ACS Nano* **13**, 1333–1341 (2019).
17. L. Novotny, N. van Hulst, Antennas for light. *Nat. Photonics* **5**, 83–90 (2011).
18. V. Giannini, A. I. Fernández-Domínguez, S. C. Heck, S. A. Maier, Plasmonic nanoantennas: Fundamentals and their use in controlling the radiative properties of nanoemitters. *Chem. Rev.* **111**, 3888–3912 (2011).
19. P. Biagioni, J.-S. Huang, B. Hecht, Nanoantennas for visible and infrared radiation. *Rep. Prog. Phys.* **75**, 024402 (2012).
20. A. G. Curto, G. Volpe, T. H. Taminiau, M. P. Kreuzer, R. Quidant, N. F. van Hulst, Unidirectional emission of a quantum dot coupled to a nanoantenna. *Science* **329**, 930–933 (2010).
21. Y. Tang, A. E. Cohen, Optical chirality and its interaction with matter. *Phys. Rev. Lett.* **104**, 163901 (2010).
22. M. Schäferling, D. Dregely, M. Hentschel, H. Giessen, Tailoring enhanced optical chirality: Design principles for chiral plasmonic nanostructures. *Phys. Rev. X* **2**, 031010 (2012).
23. Y. Tang, A. E. Cohen, Enhanced enantioselectivity in excitation of chiral molecules by superchiral light. *Science* **332**, 333–336 (2011).
24. E. Hendry, T. Carpy, J. Johnston, M. Popland, R. V. Mikhaylovskiy, A. J. Lapthorn, S. M. Kelly, L. D. Barron, N. Gadegaard, M. Kadodwala, Ultrasensitive detection and characterization of biomolecules using superchiral fields. *Nat. Nanotechnol.* **5**, 783–787 (2010).

25. A. O. Govorov, Z. Fan, P. Hernandez, J. M. Slocik, R. R. Naik, Theory of circular dichroism of nanomaterials comprising chiral molecules and nanocrystals: Plasmon enhancement, dipole Interactions, and dielectric effects. *Nano Lett.* **10**, 1374–1382 (2010).
26. X. Yin, M. Schäferling, B. Metzger, H. Giessen, Interpreting chiral nanophotonic spectra: The plasmonic Born–Kuhn model. *Nano Lett.* **13**, 6238–6243 (2013).
27. L.-Y. Wang, K. W. Smith, S. Dominguez-Medina, N. Moody, J. M. Olson, H. Zhang, W.-S. Chang, N. Kotov, S. Link, Circular differential scattering of single chiral self-assembled gold nanorod dimers. *ACS Photonics* **2**, 1602–1610 (2015).
28. H. Chen, M. Liu, L. Xu, D. N. Neshev, Valley-selective directional emission from a transition-metal dichalcogenide monolayer mediated by a plasmonic nanoantenna. *Beilstein J. Nanotechnol.* **9**, 780–788 (2018).
29. A. F. Oskooi, D. Roundy, M. Ibanescu, P. Bermel, J. D. Joannopoulos, S. G. Johnson, Meep: A flexible free-software package for electromagnetic simulations by the FDTD method. *Comput. Phys. Commun.* **181**, 687–702 (2010).
30. J. A. Schuller, S. Karaveli, T. Schiros, K. He, S. Yang, I. Kymissis, J. Shan, R. Zia, Orientation of luminescent excitons in layered nanomaterials. *Nat. Nanotechnol.* **8**, 271–276 (2013).
31. D. Vercruysse, Y. Sonnefraud, N. Verellen, F. B. Fuchs, G. Di Martino, L. Lagae, V. V. Moshchalkov, S. A. Maier, P. Van Dorpe, Unidirectional side scattering of light by a single-element nanoantenna. *Nano Lett.* **13**, 3843–3849 (2013).
32. Y. Wan, J. Xiao, J. Li, X. Fang, K. Zhang, L. Fu, P. Li, Z. Song, H. Zhang, Y. Wang, M. Zhao, J. Lu, N. Tang, G. Ran, X. Zhang, Y. Ye, L. Dai, Epitaxial single-layer MoS_2 on GaN with enhanced valley helicity. *Adv. Mater.* **30**, 1703888 (2018).
33. S. Butun, S. Tongay, K. Aydin, Enhanced light emission from large-area monolayer MoS_2 using plasmonic nanodisc arrays. *Nano Lett.* **15**, 2700–2704 (2015).
34. B. Lee, J. Park, G. H. Han, H.-S. Ee, C. H. Naylor, W. Liu, A. T. C. Johnson, R. Agarwal, Fano resonance and spectrally modified photoluminescence enhancement in monolayer MoS_2 integrated with plasmonic nanoantenna array. *Nano Lett.* **15**, 3646–3653 (2015).
35. Z. Li, Y. Li, T. Han, X. Wang, Y. Yu, B. Tay, Z. Liu, Z. Fang, Tailoring MoS_2 exciton–plasmon interaction by optical spin–orbit coupling. *ACS Nano* **11**, 1165–1171 (2017).
36. M. Amani, D.-H. Lien, D. Kiriya, J. Xiao, A. Azcatl, J. Noh, S. R. Madhvapathy, R. Addou, S. KC, M. Dubey, K. Cho, R. M. Wallace, S.-C. Lee, J.-H. He, J. W. Ager III, X. Zhang, E. Yablonovitch, A. Javey, Near-unity photoluminescence quantum yield in MoS_2. *Science* **350**, 1065–1068 (2015).
37. Z. Wu, J. Li, X. Zhang, J. M. Redwing, Y. Zheng, Room-temperature active modulation of valley dynamics in a monolayer semiconductor through chiral purcell effects. *Adv. Mater.* **31**, 1904132 (2019).
38. B. D. Busbee, S. O. Obare, C. J. Murphy, An improved synthesis of high-aspect-ratio gold nanorods. *Adv. Mater.* **15**, 414–416 (2003).
39. Y.-H. Lee, L. Yu, H. Wang, W. Fang, X. Ling, Y. Shi, C.-T. Lin, J.-K. Huang, M.-T. Chang, C.-S. Chang, M. Dresselhaus, T. Palacios, L.-J. Li, J. Kong, Synthesis and transfer of single-layer transition metal disulfides on diverse surfaces. *Nano Lett.* **13**, 1852–1857 (2013).
40. G. Lu, L. Hou, T. Zhang, J. Liu, H. Shen, C. Luo, Q. Gong, Plasmonic sensing via photoluminescence of individual gold nanorod. *J. Phys. Chem. C* **116**, 25509–25516 (2012).

Acknowledgments

Funding: This work was supported by the National Key Research and Development Program of China (grant no. 2018YFB2200401) and the National Natural Science Foundation of China (grant nos. 91950111, 61521004, and 11527901). **Author contributions:** G.L. conceived the original ideas presented in this work and constructed the experimental setup. T.W. and W.Z. performed the experiments. T.W., Y.C., and C.-W.Q. developed and performed the calculations. S.L. transferred the MoS_2 under the guidance of Y.Y. The manuscript was jointly written by T.W. and G.L. All the authors discussed the results and wrote the manuscript. **Competing interests:** The authors declare that they have no competing interests. **Data and materials availability:** All data needed to evaluate the conclusions in the paper are present in the paper and/or the Supplementary Materials. Additional data related to this paper may be requested from the authors.

Submitted 3 August 2019
Accepted 9 March 2020
Published 20 May 2020
10.1126/sciadv.aao0019

Citation: T. Wen, W. Zhang, S. Liu, A. Hu, J. Zhao, Y. Ye, Y. Chen, C.-W. Qiu, Q. Gong, G. Lu, Steering valley-polarized emission of monolayer MoS_2 sandwiched in plasmonic antennas. *Sci. Adv.* **6**, eaao0019 (2020).

ScienceAdvances

Steering valley-polarized emission of monolayer MoS_2 sandwiched in plasmonic antennas

Te Wen, Weidong Zhang, Shuai Liu, Aiqin Hu, Jingyi Zhao, Yu Ye, Yang Chen, Cheng-Wei Qiu, Qihuang Gong, and Guowei Lu

Sci. Adv., **6** (21), eaao0019.
DOI: 10.1126/sciadv.aao0019

Science Advances (ISSN 2375-2548) is published by the American Association for the Advancement of Science. 1200 New York Avenue NW, Washington, DC 20005. The title *Science Advances* is a registered trademark of AAAS.